Bio-cementation through controlled dissolution and recrystallization of calcium carbonate

Y. J. Phua and A. Røyne*

Department of Physics, University of Oslo

*Corresponding author: anja.royne@fys.uio.no

Abstract

We present an approach to bio-cementation of sand where the calcium source is prepared by dissolving powdered limestone (chalk) in lactic acid. Cementation is achieved through enzyme induced carbonate precipitation (EICP) with Jack Bean urease. The real-time nucleation and growth of crystals, crystal morphology and mechanical strength of consolidated samples was studied for dissolved chalk solution as well as calcium chloride ($CaCl_2$) and calcium lactate solutions. Solutions containing lactate were found to yield spherical calcite crystals. The compressive strengths of consolidated samples ranged from 0.06 to 2.8 MPa, increasing with the amount of precipitated $CaCO_3$.

Keywords:

Enzyme induced carbonate precipitation (EICP)

Bio-cementation

Calcite precipitation

Calcium lactate

Crystal growth

Crystal morphology

Compressive strength

1. Introduction

Cement is an important component in construction materials. It is used as a binder in concrete and as a component in mortar for masonry. The cement industry accounts for approximately 5% of global anthropogenic carbon dioxide (CO_2) emissions [1, 2]. The calcination of limestone and the combustion of fossil fuels are responsible for about 90% of CO_2 emitted from the cement industry. During the calcination process, limestone ($CaCO_3$) is thermally decomposed into lime (CaO) at high temperatures. For example, Portland cement and magnesium cement are produced by heating limestone to 1450°C and 750°C, respectively [3]. This process not only releases a lot of CO_2 from the material itself, but also involves high energy consumption.

Due to the increase in public and industrial environmental awareness, several approaches have been introduced in recent years to minimize the environmental impact caused by the cement industry. One of the most effective methods for reducing emissions and energy use in cement production today is to replace a portion of the Portland cement with pozzolanic materials of natural (volcanic) or industrial (fly ash, blast furnace slag) origin [4]. New cement materials such as energetically modified cement [5] and bio-cement [6] have also been introduced over the last few decades, in an effort to reduce the energy consumption and environmental pollution by producing cement via alternative routes.

Bio-cement is a material that is produced via a biological approach. To date, the most commonly reported system of bio-cement is based on ureolytic bacteria that produce the enzyme urease as a metabolic product. In the presence of urea and a calcium source, urease hydrolyzes urea to form ammonia and CO_2. The produced ammonia increases pH and CO_2 is transformed into carbonate ions. This leads to precipitation of calcium carbonate ($CaCO_3$). The mechanism is known as microbially induced carbonate precipitation (MICP) [7, 8]. When this takes place inside a granular material, such as sand, the formed crystals can act as a binder between grains to achieve cementation. The resulting material is a porous, sandstone-like material that can be used as bricks, for ground stabilization and could be considered for other application where low-strength concrete is used today, but should not be in direct contact with steel reinforcement due to the low pH (around 8.6) of the calcium carbonate binder.

Calcium chloride ($CaCl_2$) is often used as the calcium source in MICP. However, a major drawback of $CaCl_2$ is the excessive production of chloride ions that may lead to corrosion of the steel reinforcement used in concrete. MICP can also be achieved using other calcium salts such as calcium lactate [9, 10], calcium nitrate [9, 11, 12] and calcium acetate [10, 12], which reduce the unfavorable effects of chloride ions on concrete durability.

In search for low cost alternatives to pure calcium salts, some studies have used calcium ions from sources such as limestone [13, 14] and eggshells [15], dissolved using organic acids, for the MICP process. Limestone, which is primarily composed of $CaCO_3$, is one of the major components in conventional cement. Due to its low cost and high global abundance, it would

be a great advantage if it could be used as a major binder in concrete without the need to first decompose it at high temperatures.

In this paper, we present a two-step process to achieve cementation by dissolution and recrystallization of limestone, as illustrated in Figure 1. Our final aim is to use bacteria to both produce organic acids for limestone dissolution and urease enzyme for carbonate precipitation. However, in order to investigate the feasibility of the chemical processes involved, we present a simplified setup where we use reagent-grade lactic acid and commercial plant-derived urease from Jack Bean (*Canavalia ensiformis*).

The use of purified urease to precipitate $CaCO_3$ is known as enzyme induced carbonate precipitation (EICP). EICP offers several advantages over MICP. It eliminates the need for cultivation of, and effort to sustain, the bacteria. The use of plant-derived urease makes the system less susceptible to bio-plugging, due to its smaller size (~12 nm) [6, 7]. Furthermore, plant-derived urease is readily available in the market and will degrade after use, while in situ mirobial production of urease will leave the microorganisms behind in the material.

The process is outlined as follows (Figure 1): First, the calcium source is obtained by dissolving powdered limestone (chalk) in lactic acid to form a dissolved chalk solution (DCS):

$$CaCO_3 + \text{Lactic acid (HLact)} \rightarrow Ca^{2+} + HCO_3^- + Lact^- \quad (1)$$

Next, the DCS is mixed with equivalent amounts of urea and added into a column with sand and urease. The urease starts to hydrolyze the urea, producing bicarbonate ions and increasing pH:

$$(NH_2)_2CO + 3\ H_2O \rightarrow 2\ NH_4^+ + HCO_3^- + OH^- \quad (2)$$

This causes the dissolved $CaCO_3$ to re-precipitate:

$$Ca^{2+} + HCO_3^- + OH^- \rightarrow CaCO_3 + H_2O \quad (3)$$

In order to investigate the performance of the DCS as an alternative calcium source for bio-cementation, we also performed experiments with solutions made by dissolving commercial salts, i.e. $CaCl_2$ and calcium lactate.

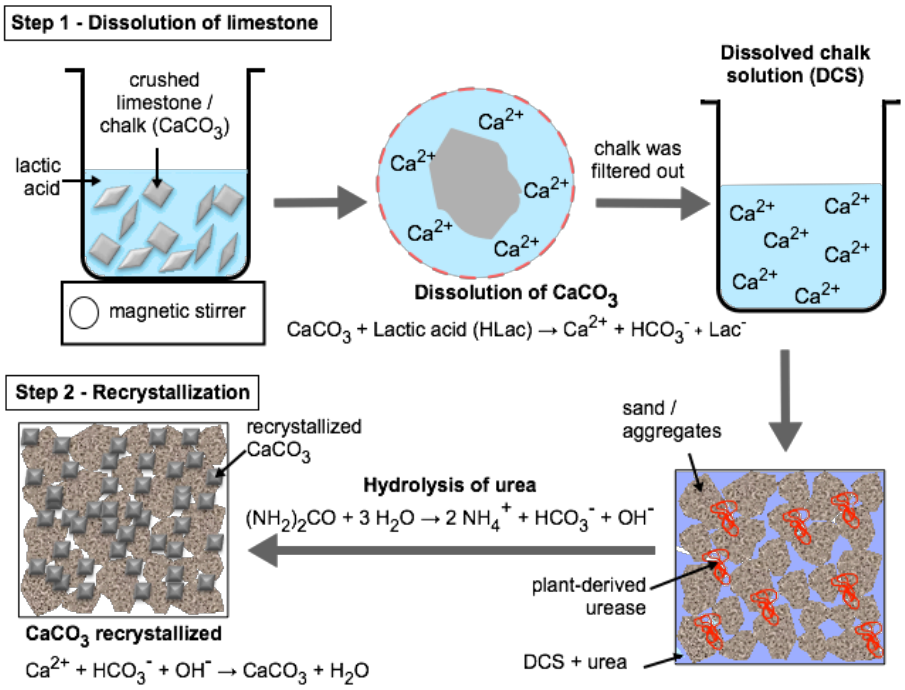

Figure 1: Illustration of cementation by dissolution and recrystallization of limestone.

In the first part of the paper, we describe real-time *in situ* monitoring of $CaCO_3$ precipitation and crystal growth from different calcium sources using an optical microscope. The structure

and morphology of the $CaCO_3$ crystals were characterized via Raman spectroscopy and scanning electron microscopy (SEM). In the second part of the paper, we report on consolidation of sand using the same approach. Different processing parameters can have substantial impact on the properties of the final consolidated product. Thus, the effects of different calcium sources and number of injections during the consolidation experiment were studied. Powdered limestone was also added in some of the samples to investigate the effects of remaining limestone particles in DCS preparation on bio-cementation. The quality of cementation was evaluated by mechanical tests of the consolidated products.

2. Materials and Methods

2.1 Materials

The powdered limestone was industrial grade chalk powder obtained from Franzefoss Miljøkalk AS (Norway) with a density of 2.7 kg/dm^3 and a particle size range of 1 - 200 μm. Sand (50 – 70 mesh particle size) from Sigma-Aldrich (USA) was used in the consolidation experiment. Jack Bean (*Canavalia ensiformis*) urease, Type IX, from Sigma-Aldrich (USA), with a specific activity of 50,000 – 100,000 units/g solid was used. Calcium chloride dihydrate was supplied by VWR Prolabo (Belgium), while calcium lactate pentahydrate and urea pellets (ReagentPlus®, purity ≥99.5%) were obtained from Sigma-Aldrich (USA).

2.2 Preparation of reagents

The dissolved chalk solution (DCS) was prepared by dissolving 25 g of powdered limestone in one liter of 300 mM lactic acid at room temperature (~21 ± 2 °C) for 24 hours. The mixture was stirred using a magnetic stirrer, and changes in pH and Ca^{2+} ion concentration

125 during the dissolution process were monitored using pH (ELIT P2011) and calcium ion
126 sensitive electrodes (ISE: ELIT 8041, PVC membrane) produced by Nico2000 (London, UK).
127 The final Ca^{2+} concentration was also measured by atomic adsorption spectroscopy (AAS,
128 Perkin Elmer AANALYST400). After completing the dissolution, the solution was filtered
129 through 11 µm pore size filter paper to remove any remaining non-dissolved limestone.
130 Calcium chloride ($CaCl_2$) and calcium lactate (CaLact) solutions were prepared by dissolving
131 the calcium salts in deionized water. Finally, urea was added to the solution, and mixed well.
132 Information about the reagents is presented in Table 1.

133

134 Table 1: Information about reagent solutions

Solution code	**Calcium source**	**Calcium (mol/l)**	**Urea (mol/l)**	**pH**
DCS	Dissolved chalk	0.065 - 0.12	0.15	6.7 ± 0.03
CaLact	CaLact	0.1	0.1	7.9
$CaCl_2$	$CaCl_2$	0.1	0.1	7.6

135

136

137 *2.3 Microscopy experiments*

138 Figure 2 shows the microscope setup used in this study. Around 10 mg of urease, in solid
139 form, was placed in the center of a glass-bottom petri dish and covered with a cover glass.
140 The gap along the edge of the cover glass was partially sealed with vacuum grease to secure
141 the position of the cover glass. 3 ml of reagents were added to the petri dish and entered the
142 gap between the cover glass and the bottom glass through capillary action. The petri dish was
143 then covered with a plastic lid to minimize evaporation of the solution. Crystallization was
144 observed with an Olympus PMG3 inverted optical microscope (Olympus, Japan) at room

temperature (~25 °C) for approximately 72 hours, and pictures were obtained with a Point Grey Grasshopper3 High Performance USB 3.0 Camera (Canada). Observations were made within the region 1 - 2 mm away from the cluster of the urease powder, which can be seen from the top view of the cover glass in Figure 2. Images were taken in time-lapse mode every minute for the first two hours, and every hour after that. After 72 hours of observations, the cover glass with precipitated crystals was rinsed with deionized water, dried, and imaged with SEM (see below).

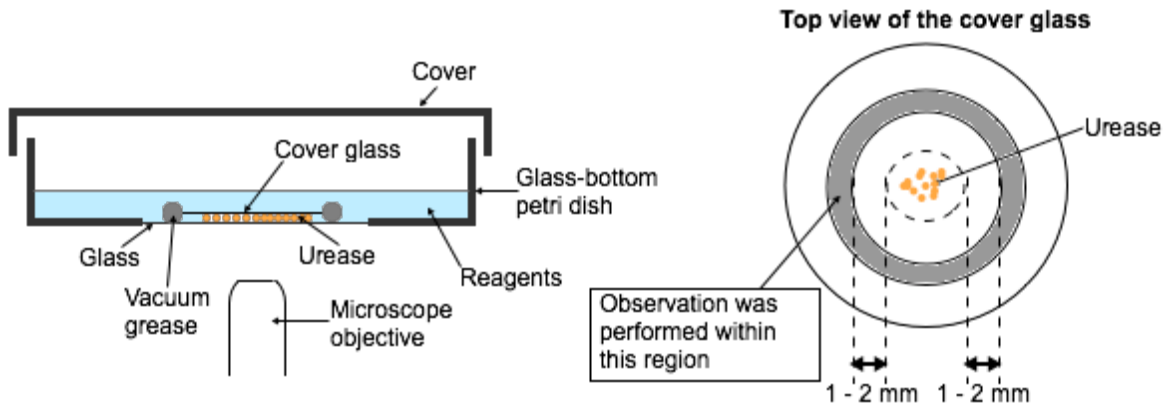

Figure 2: Microscope setup to study precipitation of $CaCO_3$

2.4 Consolidation of sand

Bio-cemented samples were prepared in a 25 mm diameter split mold (Figure 3). The two halves of the mold were held tightly together by screws. 3D printed porous flow channels and a filter paper (pore size = 11 μm) were placed in the bottom of the mold. 54 g of grains (only sand or a mixture of sand and powdered limestone; composition given in Table 2) and 0.2 g of urease were thoroughly mixed and fed into the split mold, and another filter paper and

porous flow plug was placed on top. The grains were compacted by tightening a screw and spring assemble on the top of the mold. The split mold was connected to an AL-4000 programmable double syringe pump (World of Precision Instruments, USA) at the inlet, and the outlet tube was placed in a beaker to collect the effluent fluid. The final sample height ranged from 80 to 95 mm.

To achieve cementation, 20 or 40 injections were performed at 5 hour intervals. In each step, 25 ml of reagent was injected into the mold at an injection rate of 0.5 ml/min. The reagent was pumped upwards (against gravity) through the sand in order to allow air to escape. The 5 hour interval was chosen based on the findings of Yasuhara, Neupane [16], who found that the pH of the calcium-urea-urease solutions used in a similar setting reached a steady value after 5-6 hours. In our experiments, the Ca^{2+} concentration and pH of the effluent fluid from each cycle of injections were recorded. It showed pH from pH 7.9 – pH 8.5 and Ca^{2+} ion concentration of $1 \times 10^{-3} – 8 \times 10^{-5}$ mol/l, indicating that most of the calcium had been used after 5h.

After finishing the prescribed number of injections, 50 ml of distilled water was injected into the column to wash out any soluble salts that might have formed as byproducts. Finally, the mold was split open, and the consolidated sample was removed from the mold. In order to ensure complete drying before characterization, the sample was dried in an oven at 70 °C overnight. Samples were then characterized using the methods described below. The processing conditions used are listed in Table 2 together with the sample coding. At least two samples were made for each set of processing parameters.

185

186 Table 2: Processing conditions and material designation

Sample code	Calcium source	Aggregate		Urease (g)	Number of injections	Number of samples
		Sand (wt%)	Limestone (wt%)			
sand20	DCS	100	0	0.2	20	3
sand40	DCS	100	0	0.2	40	4
90%sand20	DCS	90	10	0.2	20	3
50%sand20	DCS	50	50	0.2	20	4
sand20_CaLact	CaLact	100	0	0.2	20	2
sand20_$CaCl_2$	$CaCl_2$	100	0	0.2	20	2

187

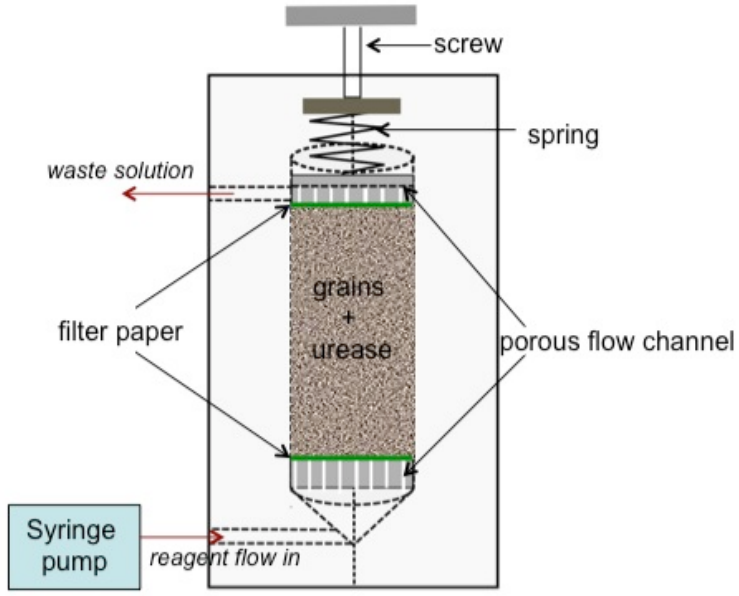

188

189 Figure 3: Illustration of the split mold setup

190

191 *2.5 Scanning Electron Microscopy (SEM)*

192 Samples from the microscopy experiments were imaged using a Hitachi SU5000 Schottky
193 field-emission scanning electron microscope (FESEM) at an accelerating voltage of 10 kV.
194 Prior to the observations, the samples were sputter-coated with a thin layer of gold to avoid
195 electrical charging during examination. Consolidated samples were imaged using a TM3000
196 tabletop microscope (bench-top SEM) from Hitachi High-Technologies. Elements present in
197 the samples were identified using Quantax70 energy dispersive spectroscopy (EDS), which is
198 an attachment to the SEM.

199

200 *2.6 Raman spectroscopy*

201 After the microscopy experiment, the cover glass with precipitated crystals was analyzed
202 using a multichannel Jobin Yvon Horiba T64000 Raman spectrometer. A Milennia Pro,
203 frequency doubled, diode-pumped ($Nd:YVO_4$ crystal) 532 nm laser from Spectra-Physics
204 (Model J 40) was used. The light was collected through a confocal microscope with an
205 Olympus 20x objective, which enabled analysis of the selected crystals. The reported spectra
206 are an average of three scans with an acquisition time of 60 seconds.

207

208 *2.7 X-Ray diffraction (XRD) analysis*

209 Crystals present in the consolidated samples were identified using Rigaku MiniFlex600 X-
210 Ray diffractometry, with a scan range from 10° - 90° and 10°/min scanning rate. The X-Ray
211 source was Cu-Kα radiation with a wavelength of 0.154 nm.

212

213 *2.8 Mechanical tests*

214 The consolidated samples were cut into half with similar height using a Discoplan-TS cutting
215 machine (Struers Inc., USA) to compare the mechanical properties of the top and bottom
216 parts of the samples. The first set of samples was subjected to uniaxial compression tests
217 using a Zwicki-line testing machine (Zwick/Roell, Germany) with a 1 kN load cell and a
218 cross-head speed of 10 mm/min. A round rubber pad with 1 mm thickness and 35 mm
219 diameter was placed on the top and the bottom of the samples assuring evenly distribution of
220 the applied forces across the sample surface. The second set of consolidated samples was
221 capped with gypsum on both ends to ensure smooth, parallel, uniform bearing surfaces that
222 were perpendicular to the applied axial load during the uniaxial compression test. The
223 specimens were subject to uniaxial compression tests using an Instron 3345 universal testing
224 machine (Instron, USA) with 5 kN load cell and a cross-head speed of 10 mm/min.

225

226 *2.9 $CaCO_3$ content measurement*

227 Portions of the consolidated samples (11 - 20 g) were dried in an oven at 70 °C for 24 hours.
228 The samples were repeatedly weighed to ensure that constant weight had been reached. Then,
229 the samples were digested in 1 M hydrochloric acid (HCl) at 40 °C under continuous stirring.
230 To ensure a full dissolution of the solid $CaCO_3$, changes in pH and Ca^{2+} ion concentration
231 was monitored by pH meter and ISE until constant values had been reached. The remaining
232 solids were filtered through filter paper, washed several times with distilled water, followed
233 by drying and re-weighing. The $CaCO_3$ content was determined as the ratio of the sample
234 weight before and after acid digestion. In samples with added limestone, the amount of
235 precipitated $CaCO_3$ was found by subtracting the initial $CaCO_3$ concentration.

236

3. Results and discussion

3.1 Dissolution of powdered limestone

During the preparation of DCS, changes in pH and Ca^{2+} ion concentration were monitored throughout the dissolution process using a pH/ISE meter. Representative curves from three different batches of DCS are presented in Figure 4. All three batches showed an increase in pH and Ca^{2+} concentration with time, but the values differed slightly from batch to batch. pH increased rapidly from ~pH 2 to ~pH 5.8 within the first 10 min after the addition of limestone to the lactic acid indicating a rapid dissolution of limestone in the initial phase. The dissolution rate then slowed down and reached pH 6.6 – pH 6.9 after 24 hours of stirring.

Also, the Ca^{2+} concentration increased rapidly during the first 10 min to around 0.01 – 0.03 mol/l, and then increased at a slower rate. The measured Ca^{2+} concentrations were slightly different in the three batches. A final Ca^{2+} ion concentration of 0.02 – 0.06 mol/l was recorded when the dissolution process was stopped after 24 hours of stirring. The final solution was also measured by atomic absorption spectroscopy (AAS) and showed a Ca^{2+} concentration ranging from 0.065 to 0.12 mol/l. The reason why the Ca^{2+} concentration measured by ISE is lower than that measured by AAS, is that lactate ions in solution complex with and chelate Ca^{2+} ions [17, 18], and the chelated calcium is no longer detectable by ISE measurement.

Calculations using PhreeqC geochemical software [19] with the *minteq* database and a K_{sp} of 3.86 for lactic acid shows that the theoretical solubility of calcium carbonate in 300 mM lactic acid is between 0.15 and 0.18 mM, depending on the amount of dissolved carbonate.

This is higher than the final Ca^{2+} concentrations we measure, indicating that the dissolution process had not reached thermodynamic equilibrium after 24 hours.

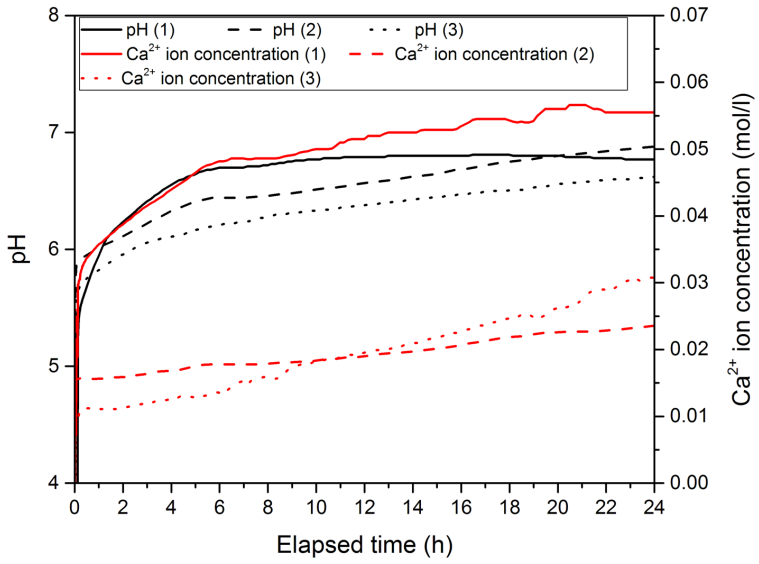

Figure 4: Changes in pH and Ca^{2+} ion concentration with time for three different dissolution batches.

3.2 Crystal growth and morphology investigations

Real-time monitoring of crystal growth was performed for up to 72 hours using the optical microscope setup shown in Figure 2. Figure 5 shows representative time-resolved microscope images of $CaCO_3$ crystal growth in $CaCl_2$-solution, CaLact-solution and DCS. Based on the collected images, the crystal growth rate was assessed by analyzing the fraction of the field of view covered by crystals every 2 hours, as presented in Figure 6.

In all solutions, precipitation of $CaCO_3$ occurred rapidly. Visible crystals appeared in the solution around 10 minutes after the reagents were added (not shown in the figures). In the

275 $CaCl_2$ solution, numerous rhombohedral calcite crystals precipitated in the initial stage and
276 grew rapidly during the first 4 hours. After that, the growth slowed down to a very low,
277 almost steady rate for the remaining hours.

278

279 In the CaLact and DCS solutions, nucleation appeared to be slower. There were fewer
280 crystals present after 2 hours, and new crystals still appeared after 4 hours. The decrease in
281 growth rate with time was slower than in the $CaCl_2$ solution. In the CaLact solution, a
282 mixture of rhombohedral and spherical shaped crystals was formed, while there were mainly
283 spherical shaped crystals in the DCS solution.

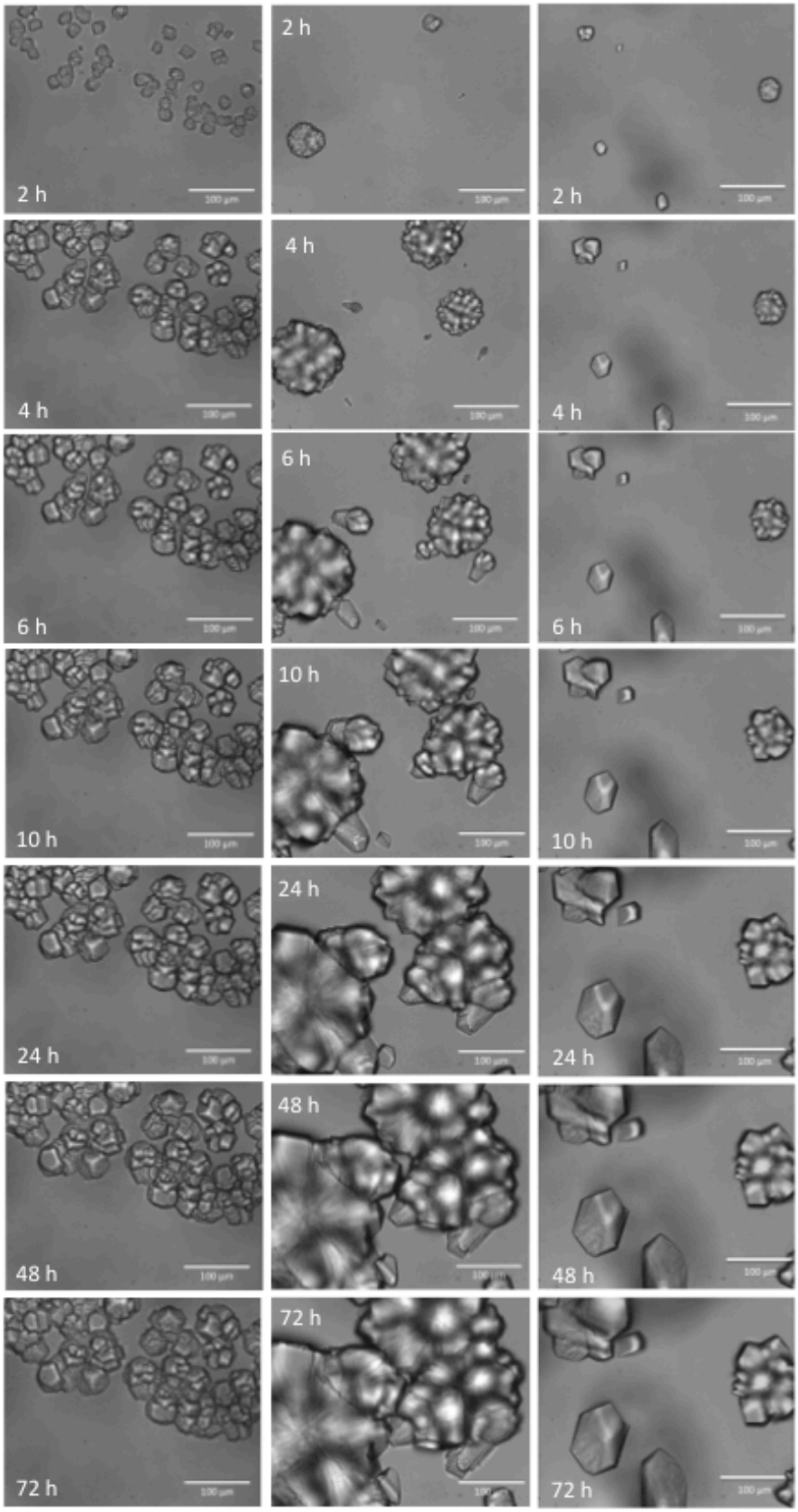
2 h
2 h
2 h
4 h
4 h
4 h
6 h
6 h
6 h
10 h
10 h
10 h
24 h
24 h
24 h
48 h
48 h
48 h
72 h
72 h
72 h
CaCl2
CaLact
DCS

284

285 Figure 5: Representative time-resolved microscope images of $CaCO_3$ crystals formed in
286 $CaCl_2$- and CaLact solutions and DCS

287

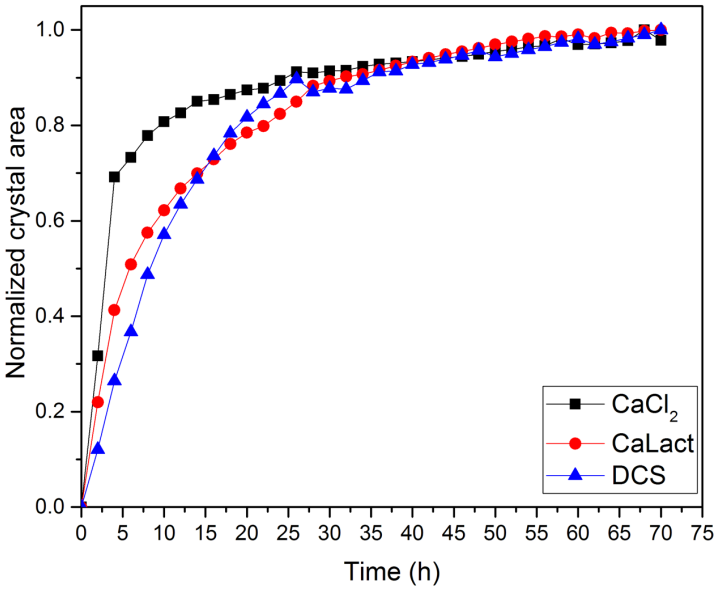

288

289 Figure 6: Fraction of area seen in the microscope that is covered by crystals as a function of
290 time and calcium solution. The curves are normalized to the final value.

291

292 The precipitated $CaCO_3$ crystals were studied by SEM. Using $CaCl_2$ as calcium source the
293 precipitate consisted of 20 - 80 µm rhombohedral $CaCO_3$ crystals (Figure 7), which is the
294 typical morphology of calcite. Some of the crystals exhibited smooth crystal faces with
295 sharply defined edges, but most of the crystals had only partly developed smooth faces and
296 incompletely formed edges, and appeared as clusters of inter-grown crystals (Figure 7b).
297 $CaCl_2$ is the most commonly used calcium source in MICP and EICP studies [8, 16]. Similar
298 observations were reported in those studies, where rhombohedral calcite precipitated [16, 20,
299 21].

300

301 On the other hand, in the CaLact sample, spherical shaped $CaCO_3$ crystals with a diameter of
302 100 - 250 μm was the dominant morphology (Figure 8). A close-up of the spherical crystals
303 at higher magnification (Figure 8b) showed that the spheres appeared to be spherical
304 aggregates of smaller rhombohedral sub-units of 10 - 50 μm size. Other researchers have
305 reported similar $CaCO_3$ crystal morphology, which is known as calcite spherulites [22-24].
306 These studies used $CaCl_2$ as calcium source, but had bacteria or other impurities present in
307 the system. In our experiments, the precipitated calcite spherulites had a larger overall size
308 than the rhombohedral calcite crystals that were precipitated from the $CaCl_2$ solution. Similar
309 calcite spherulites were found in the sample using DCS as calcium source, the diameter was
310 similar to those precipitated from the CaLact solution (100 - 250 μm). Rhombohedral calcite
311 crystals were also detected in the sample, but calcite spherulite was the dominating
312 morphology of the precipitated crystals.

313

314 Several mechanisms have been proposed to explain the formation of calcite spherulites. Al-
315 Thawadi and Cord-Ruwisch [23] studied the formation of calcite spherulites by ureolytic
316 bacteria in an MICP process. They suggested that, initially, spherical shaped vaterite crystals
317 were formed, these however, gradually disintegrated and transformed into rhombohedral
318 calcite (after 9 hours), inheriting the spherical shape of the initial vaterite spheres. In our
319 study, no signs of vaterite formation were observed under the microscope nor in SEM and
320 XRD analysis (see later). Instead, as seen in Figure 5, calcite spherulites appeared from the
321 beginning of crystal formation, and increased their size radially with time. Hence, the concept
322 of spherulitic growth of $CaCO_3$ as described by Beck and Andreassen [25] is a more likely
323 mechanism to explain the formation of calcite spherulites in our system. An array of

crystalline subunits (here: rhombohedral calcite) grows multidirectionally from a common precursor, leading to the formation of calcite spherulites. Spherulitic growth of calcite can be due to the presence of impurities, organic molecules, or other static heterogeneities like phase separation in the system [22, 25, 26]. Presumably, the presence of lactate is the main reason of calcite spherulite formation in our system.

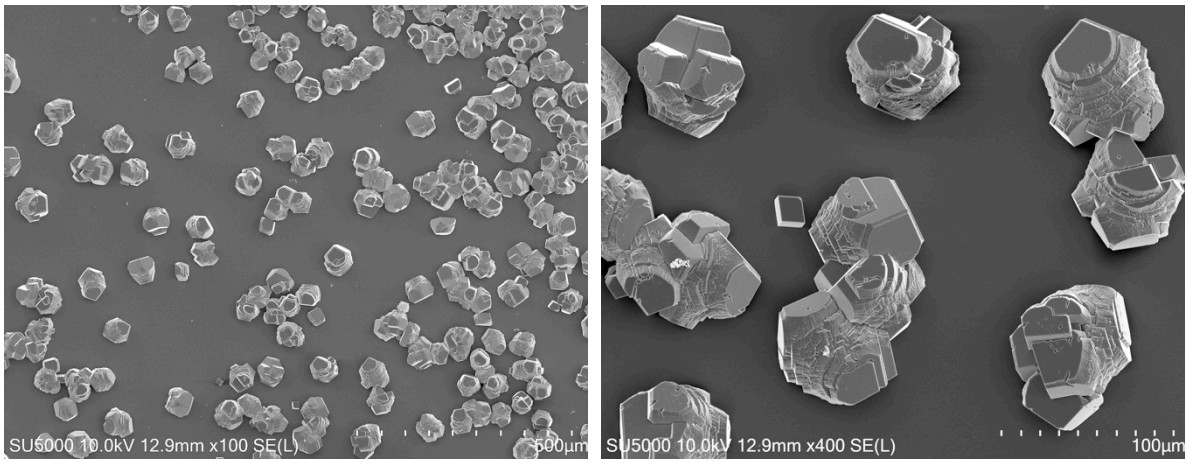

(a) (b)

Figure 7: SEM images of $CaCO_3$ crystals formed in 0.1M $CaCl_2$ solution, a) at 100 x magnification and b) at 400 x magnification.

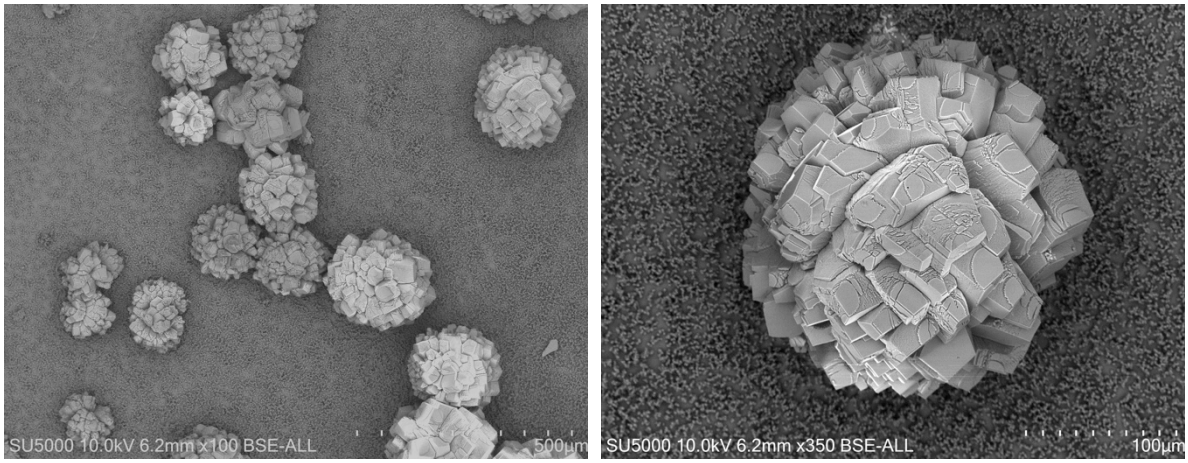

(a) (b)

333 Figure 8: SEM images of $CaCO_3$ crystals formed in 0.1M CaLact solution, a) at 100 x
334 magnification and b) at 350 x magnification.

335

336

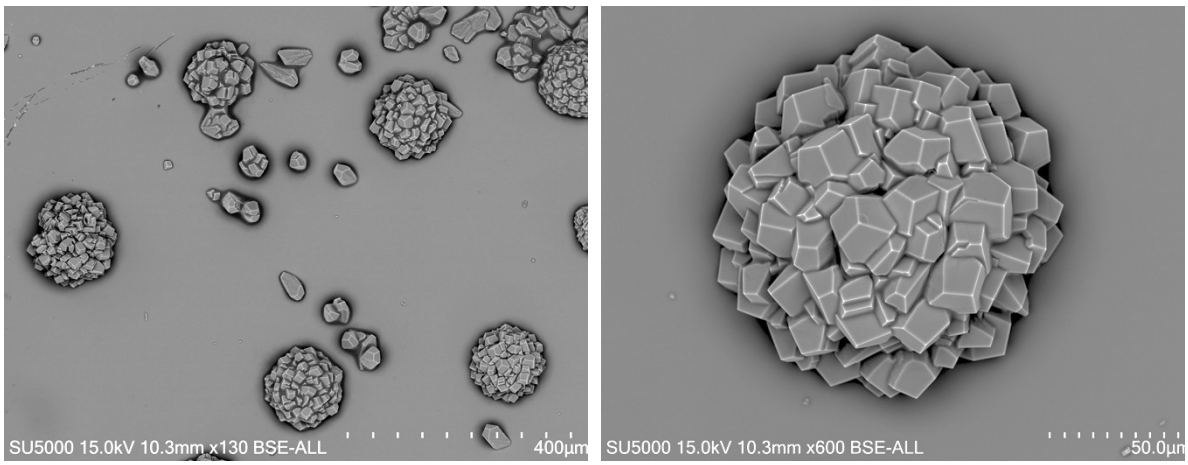

(a) (b)

337

338 Figure 9: SEM images of $CaCO_3$ crystals formed in DCS, a) at 130 x magnification and b) at
339 600 x magnification.

340

341 In order to confirm the identity of the precipitated crystals, Raman spectroscopy was
342 performed (Figure 10). Both the rhombohedral calcite obtained by precipitation from $CaCl_2$-
343 solution and the calcite spherulites obtained by precipitation from CaLact-solution and DCS
344 showed identical Raman spectra that corresponded to the characteristic peaks of calcite. The
345 peak at 288 cm^{-1} arises from the external vibrations of the CO_3^{2-} groups that involve rotatory
346 oscillations of those groups. A weak peak at 716 cm^{-1} is attributed to symmetric deformation
347 of CO_3 groups. The symmetric stretching of CO_3 groups show a strong Raman band at 1092
348 cm^{-1} [27]. This verifies that all crystals were calcite but with different morphologies.

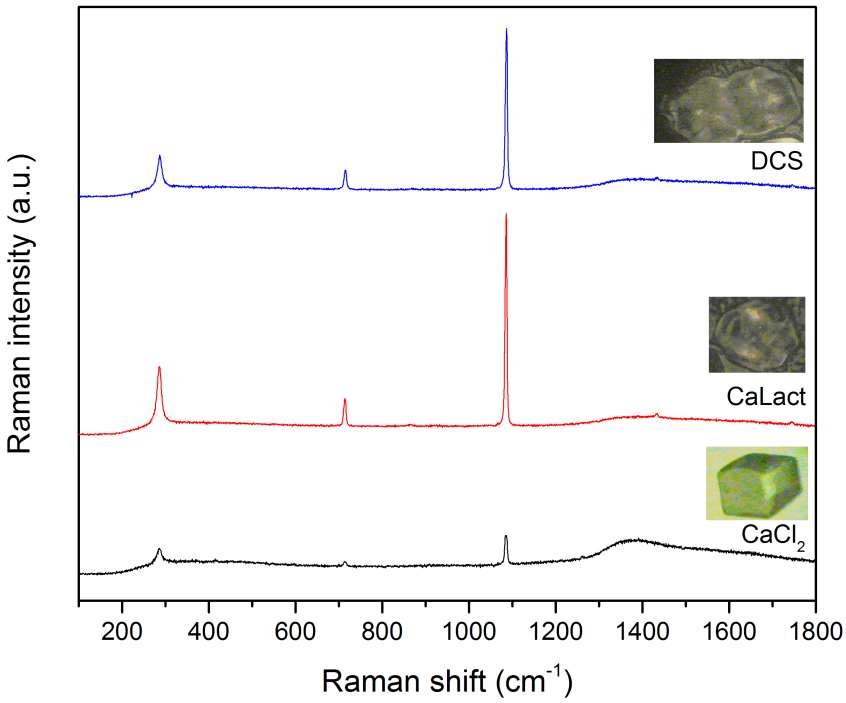

349

350 Figure 10: Raman spectra of crystals precipitated from DCS and $CaCl_2$- and CaLact-solutions.

351

352 *3.3 Consolidation of sand*

353 Consolidated, cylindrical samples were obtained using the preparation procedure described
354 above. A typical image of a consolidated sample (before cutting) is shown in Figure 11. The
355 samples were all well cemented, and did not disintegrate in water. This shows that
356 consolidation of sand can be achieved through EICP using different calcium sources and
357 processing parameters.

358

359

360 Figure 11: Typical image of a consolidated sand sample made from DCS.

361

362 *3.4 Crystal morphologies of the consolidated samples*

363 SEM images (Figure 12) of the consolidated sand samples prepared from different processing
364 conditions showed that calcite crystals precipitated on free surfaces and between the sand
365 grains. The latter acted as a cement to bind the sand grains together. The precipitated calcite
366 crystals in the consolidated sand samples had the same morphology as observed in the
367 microscope experiments. The $CaCl_2$ solution yielded typical rhombohedral calcite crystals,
368 while a large fraction of the precipitated calcite crystals from DCS and calcium lactate
369 solution were calcite spherulites.

370

For the 90%sand20 and 50%sand20 samples (Table 2), 10 and 50 weight% of sand was replaced by powdered limestone, respectively. A similar cementation effect is observed from the SEM images (Figures 12e and 12f), in which the precipitated calcite crystals act as a binder to bind the grains together. Both the precipitated crystals and the added limestone are calcite, and they can therefore be difficult to distinguish. In Figure 12e, two distinct morphologies of calcite were detected. Powdered limestone is known to have a rhombohedral morphology and often with faceted surfaces (as labeled in the figure). Meanwhile, the precipitated crystals appear as a cluster of smaller crystals similar to those observed in sand20 and sand40 samples, but not in a spherical orientation. This can be confirmed by a visible hole that is created by a pulled-out sand grain in Figure 12e, where the precipitated small calcite crystals formed an aggregate and covered the sand grain. For 50%sand20 sample (Figure 12f), the calcite crystals are difficult to distinguish, because the amount of added limestone is much higher than the amount of precipitated calcite.

In the samples with added limestone, the presence of calcite spherulites were not detected. Differences in calcite morphology between sand and sand-limestone systems are probably due to differences in the number of potential nucleation sites. It is likely that limestone possesses more favorable nucleation sites for calcite precipitation, allowing nucleation to occur simultaneously at multiple sites. This results in the formation of many small calcite crystals in different places, subsequently prohibiting the spherulitic growth of calcite.

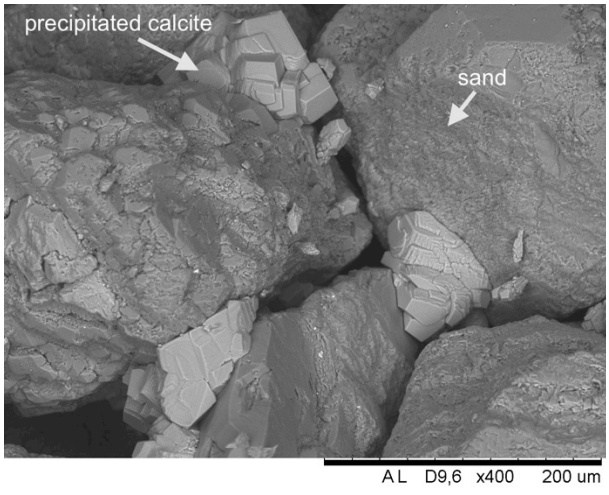
precipitated calcite
sand
AL D9,6 x400 200 um

(a)

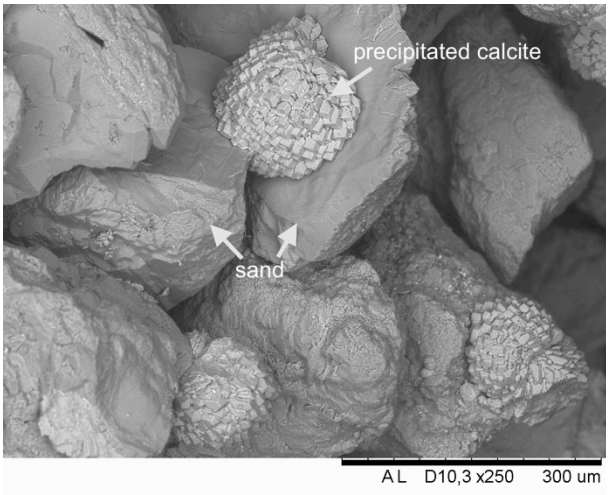
precipitated calcite
sand
AL D10,3 x250 300 um

(b)

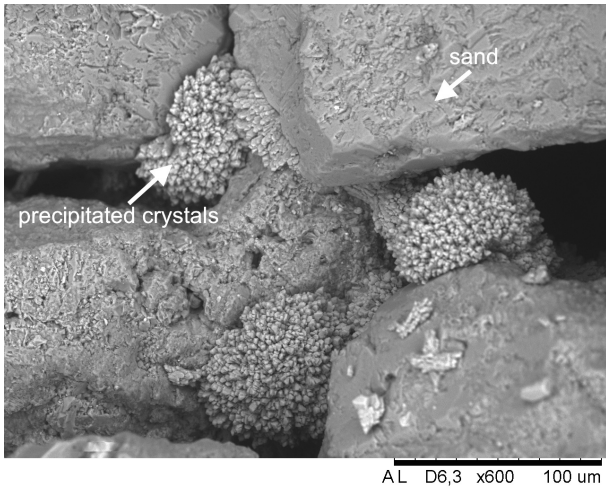
sand
precipitated crystals
AL D6,3 x600 100 um

(c)

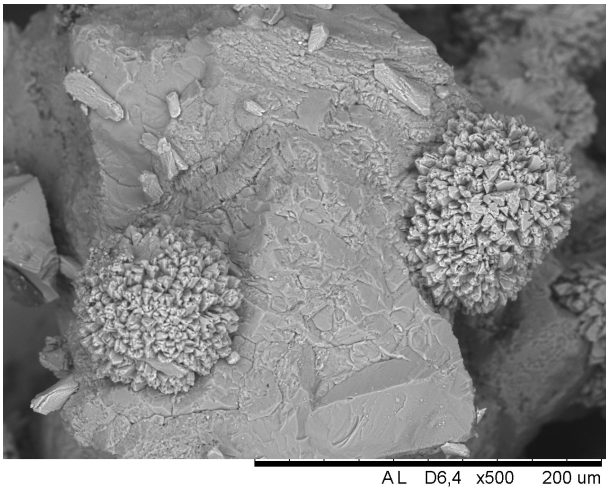
AL D6,4 x500 200 um

(d)

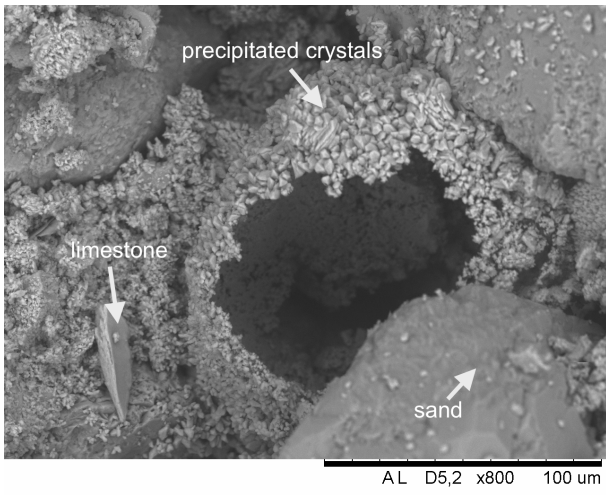
precipitated crystals
limestone
sand
AL D5,2 x800 100 um

(e)

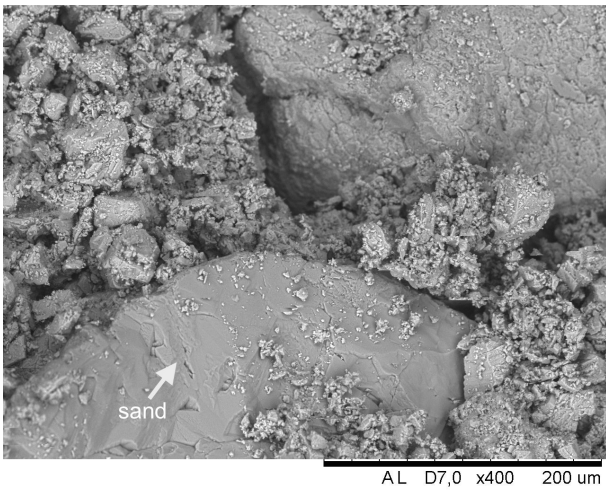
sand
AL D7,0 x400 200 um

(f)

391 Figure 12: SEM images of consolidated sand samples: (a) sand20_$CaCl_2$, (b) sand20_CaLact
392 and (c) sand20, (d) sand40, (e) 90%sand20 and (f) 50%sand20 (note that the magnifications
393 of the images are different).

394

395 *3.5 Elemental analysis and phase identification*

396 Elements present in the sand20 sample were identified using EDS mapping. The distribution
397 of the different elements in the framed area is illustrated in Figure 13. Large grains that
398 contained silicone (Si) and oxygen (O) correspond to sand (quartz, SiO_2). The spherical shape
399 crystal aggregates contained calcium (Ca), carbon (C) and O and assumed to be $CaCO_3$. This
400 was confirmed by XRD analysis (Figure 14). Other polymorphs of $CaCO_3$, such as vaterite
401 and aragonite, were not detected.

402

403

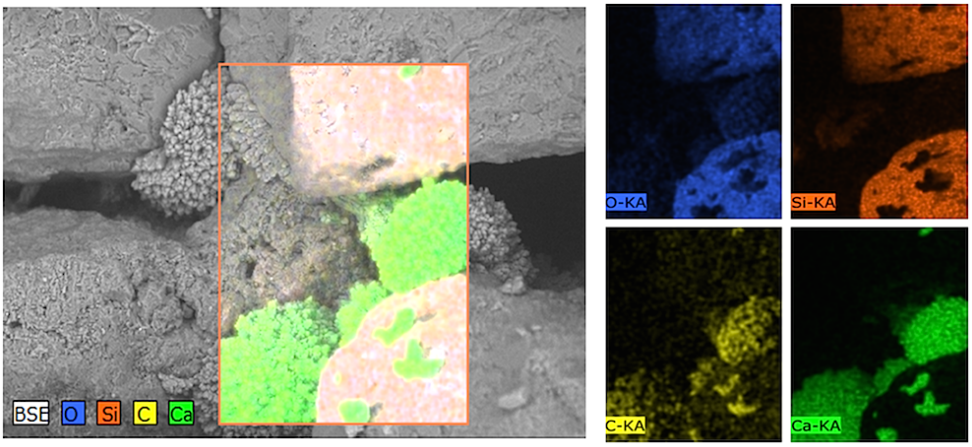

404

405 Figure 13: Elemental mapping of sand20 sample using EDS.

406

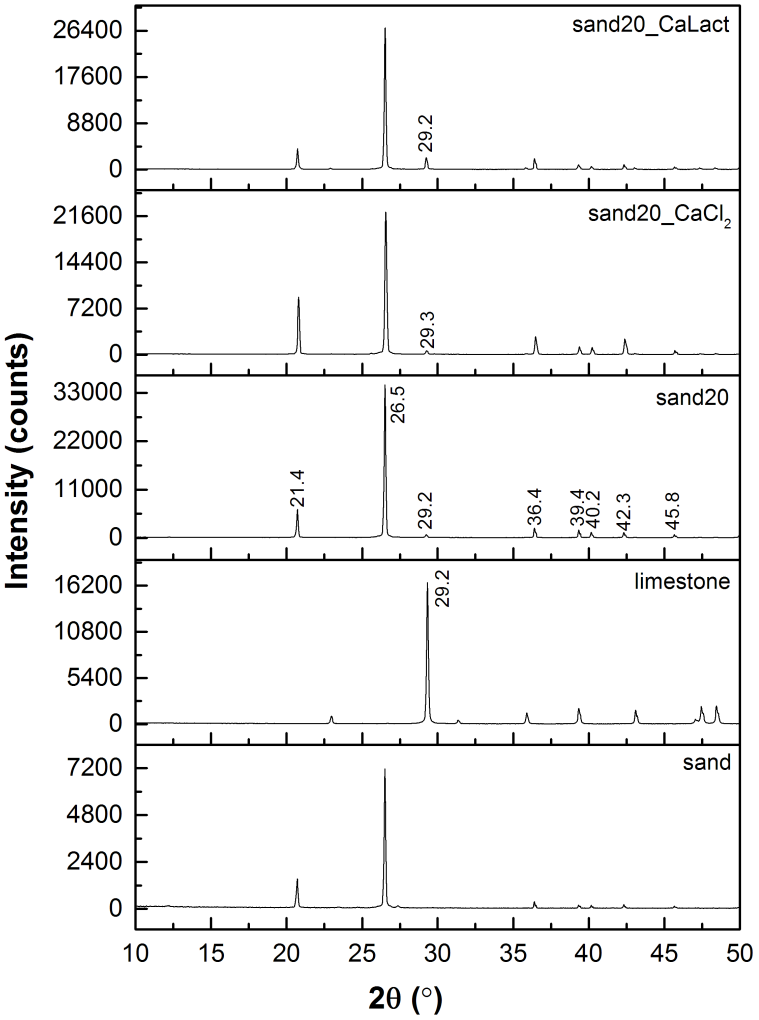

407

408 Figure 14: XRD patterns of sand, limestone and consolidated samples.

409

410 *3.6 $CaCO_3$ content*

411 The consolidated samples were cut horizontally into half along the middle plane, to compare
412 their properties in the top and bottom portions. As described in the experimental procedures,
413 reagents were pumped upward into the mold during the production. Thus, the bottom half is
414 closest to the injection inlet and the top half furthest from the injection inlet. Results (Table 3)
415 show that the bottom samples contain a higher amount of precipitated $CaCO_3$ than the top
416 samples, suggesting that more precipitation occurred near the inlet region.

417

418 The precipitation of $CaCO_3$ is influenced by the processing parameters, including the
419 concentration of Ca^{2+} and urea, the amount of urease, and the number of injections [8, 28].
420 As expected, the sand40 samples subjected to 40 injections, contained more precipitated
421 $CaCO_3$ than samples with 20 injections (Table 3). However, the amount of precipitated
422 $CaCO_3$ in the sand40 samples was less than twice as much as in the sand20 samples,
423 indicating that the urease activity in the system declined with time, probably due to enzyme
424 inactivation or washout. There is also a large spread in the average $CaCO_3$ content in sand40
425 samples due to leakage of the mold during the production of two of the samples. The two
426 sand40 samples that did not experience leakage had an average precipitated $CaCO_3$ content as
427 high as 16 – 17 %. The same leakage problem also occurred for two of the 50%sand20
428 samples, and led to high standard deviation in the results.

429

430 The samples with added limestone had a slightly lower precipitated $CaCO_3$ content than the
431 corresponding pure sand samples. This was not as expected, as the presence of limestone
432 increases the nucleation of calcite crystals in the system. As none of the molds were perfectly
433 sealed, we suspect that the lower amount of precipitation in the samples containing limestone
434 was due to a lower initial permeability of these samples, which resulted in a higher injection
435 pressure and therefore more leakage.

436

437 The amounts of precipitated $CaCO_3$ using CaLact and $CaCl_2$ solutions were almost equal,
438 presumably because they contained identical concentrations of calcium and urea. This shows

439 that the calcium source in this case did not significantly affect the rate or amount of
440 precipitation.

441

442 Table 3: Precipitated $CaCO_3$ in consolidated sand columns made under different processing
443 conditions. Numbers shown are averages and standard deviations for 3 or 4 replicates (Table
444 2), except for the sand20_$CaCl_2$ and sand20_CaLact samples where material from the
445 duplicates was mixed after compression tests, and only one measurement was made.

Sample	**Average $CaCO_3$ content (wt%)**		**Theoretically expected $CaCO_3$ precipitation (wt%)**
	Top sample	**Bottom sample**	
sand20	11.1 ± 1.0	13.7 ± 1.9	5.7 – 10.0
sand40	13.5 ± 3.5	14.1 ± 4.5	11.4 – 20.0
90%sand20	9.4 ± 1.3	11.6 ± 0.7	5.7 – 10.0
50%sand20	6.9 ± 3.9	9.8 ± 6.6	5.7 – 10.0
sand20_$CaCl_2$	6.6	8.3	8.5
sand20_CaLact	7.7	8.5	8.5

446

447 The theoretically expected $CaCO_3$ content, based on the amount of Ca^{2+}-ions added during
448 the consolidation process, was calculated (Table 3). Twenty injections correspond to a total
449 injected volume of 500 ml calcium solution containing 0.05 moles of Ca^{2+} ions and other
450 dissolved Ca-species for the $CaCl_2$ and the CaLact solutions, and 0.0325 moles of Ca^{2+} ions
451 for the DCS. Theoretically, DCS may have contained up to 0.15 moles of dissolved Ca-
452 species per liter, corresponding to an addition of 0.075 moles of dissolved Ca-species during
453 the consolidation process. Precipitation of 1 mole of $CaCO_3$ requires 1 mole of Ca^{2+} ions, and
454 the theoretical maximum $CaCO_3$ content in the consolidated sand columns is given by
455 $nM_c/(m_a+nM_c)$, where n is the expected number of moles of precipitated $CaCO_3$, M_c is the

456 molar mass of $CaCO_3$ (100.09 g/mol), and m_a is the mass of the aggregate (sand + limestone)
457 in each prototype (54 g).

458

459 For the $CaCl_2$ and CaLact samples, the $CaCO_3$ contents of the bottom samples were in good
460 agreement with the theoretical prediction, while the top samples were slightly lower.
461 However, all of the DCS samples had a higher $CaCO_3$ content than expected based on the
462 Ca^{2+} concentrations measured by AAS. If the dissolution process had reached
463 thermodynamic equilibrium, then assuming a calcite solubility of 0.18 M Ca^{2+}, the expected
464 $CaCO_3$ content should have been 14.3%. This is higher than most observed values. One
465 possible reason for the discrepancy between the Ca^{2+} content measured by AAS and the
466 amount of precipitated material is that tiny particles of powdered limestone remain in the
467 DCS after filtration, and continue to be dissolved until the solution reaches thermodynamic
468 equilibrium, so that the actual Ca^{2+} content in the injected solution is higher than what was
469 measured.

470

471 *3.7 Mechanical properties*

472 The compressive strengths of the consolidated samples were evaluated by a uniaxial
473 compression test, and the results are presented in Figure 15. In this test, it is essential to
474 assure that the applied force is evenly distributed to the sample. The first batch of samples
475 were tested using 1 mm-thick rubber pads that were placed on top and bottom of the samples
476 to ensure uniform force distribution (Figure 16a). Another set of consolidated samples made
477 from DCS were subjected to another testing method, in which gypsum capping was applied at

478 both ends of the samples to create smooth and parallel surfaces that were perpendicular to the
479 applied axial load during the uniaxial compression test (Figure 16b).

480

481 The observed compressive strength ranged from 0.06 to 2.8 MPa. The higher values were
482 comparable to soft rocks such as sandstone and siltstone [29]. In general, the bottom samples
483 displayed higher compressive strengths than the top samples. This can be attributed to the
484 greater amount of $CaCO_3$ precipitation near the inlet, as shown by the $CaCO_3$ content
485 measurements (Table 3). The trend for all samples was that the compressive strength
486 increased strongly with the content of precipitated $CaCO_3$ (Figure 15). This is in agreement
487 with how the compressive strength of porous concrete depends on the porosity and on the
488 total area of solid-solid contact [30, 31].

489

490 The consolidated samples produced with DCS had a higher $CaCO_3$ content and higher
491 strength than those made from $CaCl_2$ and CaLact solutions. However, when comparing
492 strength as a function of $CaCO_3$ content, the $CaCl_2$ and CaLact samples seem to perform
493 slightly better than the DCS samples.

494

495 Addition of chalk did not significantly alter the mechanical strength of the consolidated
496 samples. The average compressive strength of the 90%sand20 and the 50%sand20 samples
497 were lower than that of the sand20 sample. The degree of $CaCO_3$ precipitation was also lower
498 in the samples with added limestone (as shown in Table 3), probably due to leaks. In the
499 mixtures of sand and chalk, the grain size distribution was wider than for pure sand. One
500 could expect that the presence of small chalk grains that can fill up the space between the

sand grains would increase the area of solid-solid contact and therefore result in a higher compressive strength for a given amount of precipitated material. However, the morphology of the precipitated $CaCO_3$ was also different in the samples with chalk. The samples with only sand contained precipitated calcite spherulites, while the samples with chalk contained smaller, more dispersed aggregates of calcite crystals (Figure 12). The strength of bio-cemented sand is expected to depend on to what degree the precipitated calcite crystals are able to form bridges between the adjacent sand grains [32]. The lack of increased strength in chalk containing samples could be due to a better binding efficiency of the calcite spherulites, through creating a larger contact area between sand grains, compared with multiple small crystals scattered on the grain surfaces.

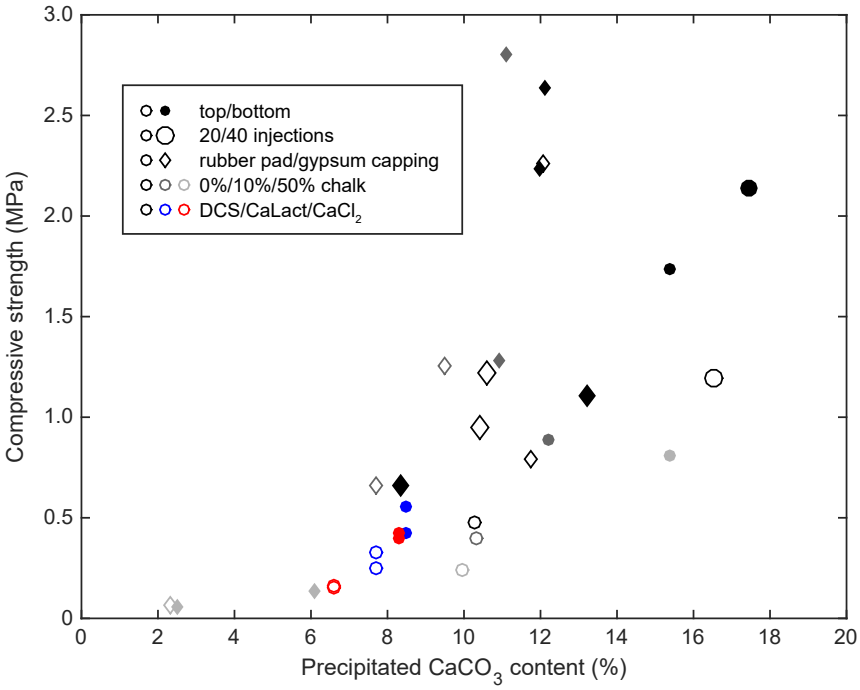

514 Figure 15: Compressive strength of all samples as a function of precipitated $CaCO_3$ content.
515 Data for gypsum capping are the results of single measurements, while data for the rubber
516 pad are averages over several replicates.

517

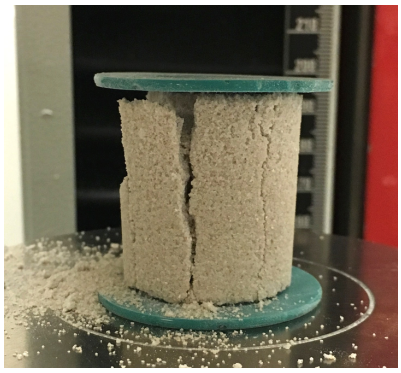

(a)

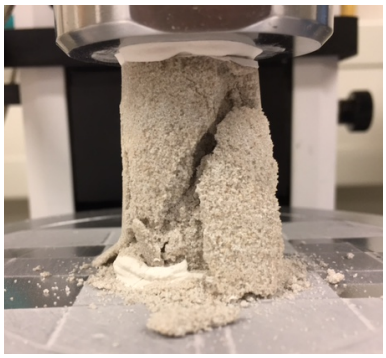

(b)

518 Figure 16: Axial splitting in a rubber pad test (a) and shear failure in a gypsum-capped
519 sample (b) observed on sand20 samples under uniaxial compression.

520

521 In order to investigate the effect of the testing method, we can compare the mechanical test
522 results for the sand20 and the 90%sand20 samples. These samples had very similar $CaCO_3$
523 content (Table 3) and were therefore expected to have similar mechanical strength. However,
524 the strength of the gypsum-capped samples was higher than that measured for the rubber pad
525 samples. The lower strength obtained with the rubber pad was probably a result of tensile
526 stresses normal to the loading direction, set up by lateral extension of the rubber, which
527 resulted in axial splitting of the samples (Figure 16a). The stress-strain curves of the selected
528 samples (Figure 17) showed a significant effect of the presence of the rubber pads both on the
529 measured elastic modulus and the failure behavior. The gypsum capped samples displayed
530 shear failure (Figure 16b) at a higher measured load. The latter is probably a more

representative measure of the compressive strength of the samples, and we expect that the actual strength of the samples tested using rubber pads is around 50% higher than reported in Figure 15.

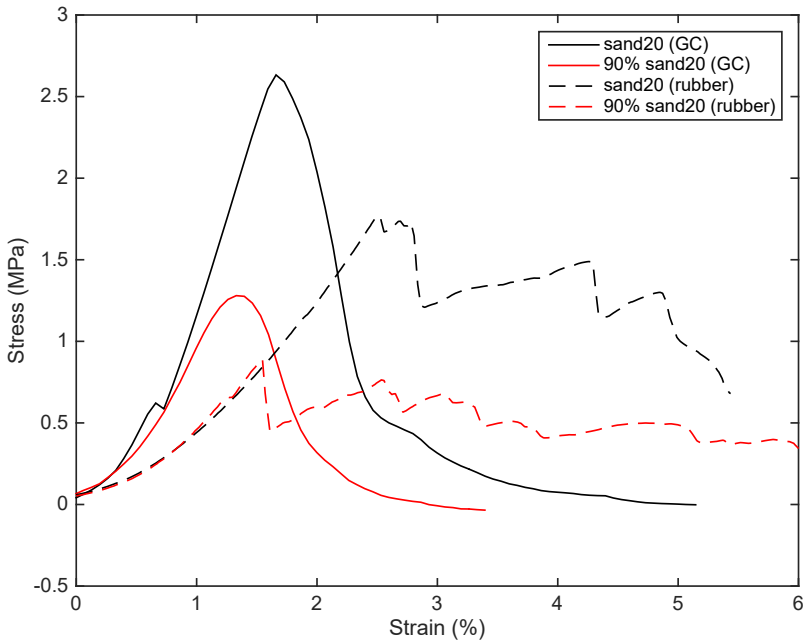

Figure 17: Typical stress-strain curves of sand20 (black) and 90%sand20 (red) bottom samples that were tested using gypsum capping (solid lines) and rubber pad (dashed lines).

4. Conclusions

Enzymatically induced precipitation (EICP) of $CaCO_3$ was achieved using solutions of calcium chloride, calcium lactate and powdered limestone dissolved in lactic acid (DCS) as calcium sources. The morphology of the precipitated $CaCO_3$ crystals depended on the calcium source. Rhombohedral calcite crystals were formed in the $CaCl_2$ solution, while calcite spherulites were formed in the DCS and the Ca-Lactate solutions. Real-time monitoring of crystal growth showed that the spherulites were formed at the initial stages of crystallization and grew radially with time, suggesting that they were not formed by a

546 transformation from spherical vaterite to calcite. Presumably, the presence of lactate induced
547 the formation of calcite spherulites.

548

549 Cylindrical samples of consolidated sand, or sand mixed with limestone powder, were
550 produced using EICP and the different calcium solutions. The morphology of the precipitated
551 $CaCO_3$ crystals in the consolidated samples were similar to those observed under the
552 microscope when $CaCO_3$ was precipitated from the same calcium solutions, but the presence
553 of limestone powder gave rise to smaller, more scattered precipitates. The compressive
554 strength of the consolidated samples increased with increasing content of precipitated $CaCO_3$.
555 More $CaCO_3$ precipitation was detected in the region closest to the injection inlet and yielded
556 a higher strength. The presence of limestone powder did not significantly affect the
557 compressive strength of the samples, probably due to competing effects of a wider grain size
558 distribution and smaller, more scattered precipitated crystals.

559

560 In general, our results demonstrate the feasibility of using limestone powder dissolved in
561 lactic acid as a calcium source for bio-cementation purposes.

562

563 **Acknowledgements**

564 This work was supported by the Norwegian Research Council [grant number 238849]. We
565 thank the following people for technical assistance: Berit Løken Berg (SEM), Niels Højmark
566 Andersen (Raman microscopy), Grazyna Jonski (AAS), Michaela Meir and Jonas
567 Wengenroth (mechanical tests, and David Wragg (XRD). The authors would also like to
568 thank the BioZEment consortium, specifically Alexander Wentzel, Simone Balzer Le, Sidsel

569 Markussen, Kjell Domaas Josefsen, Pawel Sikorski, Harald Throne-Holst, Anita Borch, Frida
570 Røyne, and Anders Myhr for their ideas, constructive discussions and feedback on the
571 manuscript.

572

573 **References**

574 1. Sabnis, G.M., Green Building with Concrete: Sustainable Design and Construction,
575 Second Edition. 2015: CRC Press.

576 2. Calkins, M., Materials for Sustainable Sites: A Complete Guide to the Evaluation,
577 Selection, and Use of Sustainable Construction Materials. 2008: Wiley.

578 3. Smith, P.F., *Architecture in a Climate of Change*. 2006: Taylor & Francis.

579 4. Aïtcin, P.-C. and S. Mindess, *Sustainability of Concrete*. 2011, Oxon, UK: Spon
580 Press.

581 5. Justnes, H., L. Elfgren, and V. Ronin, *Mechanism for performance of energetically*
582 *modified cement versus corresponding blended cement.* Cement and Concrete Research,
583 2005. **35**(2): p. 315-323.

584 6. Ariyanti, D. and N.A. Handayani, *Feasibility of using microalgae for biocement*
585 *production through biocementation.* Journal of Bioprocessing & Biotechniques, 2013.
586 **2012**.

587 7. Achal, V. and A. Mukherjee, *A review of microbial precipitation for sustainable*
588 *construction.* Construction and Building Materials, 2015. **93**: p. 1224-1235.

589 8. De Muynck, W., N. De Belie, and W. Verstraete, *Microbial carbonate precipitation*
590 *in construction materials: A review.* Ecological Engineering, 2010. **36**(2): p. 118-136.

591 9. Xu, J., et al., Effects of Calcium Source on Biochemical Properties of Microbial
592 CaCO(3) Precipitation. Frontiers in Microbiology, 2015. **6**: p. 1366.

593 10. Gorospe, C., et al., Effects of different calcium salts on calcium carbonate crystal
594 formation by Sporosarcina pasteurii KCTC 3558. Biotechnology and Bioprocess
595 Engineering, 2013. **18**(5): p. 903-908.

596 11. Sun-Gyu, C., N. In-Hyun, and P. Sung-Sik, Effect of Plant-Induced Calcite
597 Precipitation on the Strength of Sand. 2014.

598 12. Zhang, Y., H.X. Guo, and X.H. Cheng, *Role of calcium sources in the strength and*
599 *microstructure of microbial mortar.* Construction and Building Materials, 2015. **77**: p.
600 160-167.

601 13. Choi, S.-G., et al., Sustainable biocement production via microbially-induced
602 calcium carbonate precipitation: use of limestone and acetic acid derived from pyrolysis
603 of lignocellulosic biomass. ACS Sustainable Chemistry & Engineering, 2017.

604 14. Chu, J. and Z. Wen, Proof of Concept: Biocement for Road Repair. 2015.

605 15. Choi, S.-G., S. Wu, and J. Chu, *Biocementation for Sand Using an Eggshell as*
606 *Calcium Source.* Journal of Geotechnical and Geoenvironmental Engineering, 2016.
607 **142**(10): p. 06016010.

608 16. Yasuhara, H., et al., Experiments and predictions of physical properties of sand
609 cemented by enzymatically-induced carbonate precipitation. Soils and Foundations,
610 2012. **52**(3): p. 539-549.

611 17. Nawab, Z., et al., Calcium-complexing versus vasorelaxant effect of acetate,
612 lactate, and other bases. ASAIO Journal, 1984. **30**(1): p. 184-188.

18. Zander, R. and D.J. Cooper, *Association between plasma ionized calcium and lactate concentration.* Intensive Care Medicine. **19**(6): p. 362-363.

19. Parkhurst, D.L. and C.A.J. Appelo, Description of input and examples for PHREEQC version 3—A computer program for speciation, batch-reaction, one-dimensional transport, and inverse geochemical calculations, in U.S. Geological Survey Techniques and Methods, book 6. 2013.

20. Abo-El-Enein, S.A., et al., Utilization of microbial induced calcite precipitation for sand consolidation and mortar crack remediation. HBRC Journal, 2012. **8**(3): p. 185-192.

21. De Muynck, W., et al., Influence of urea and calcium dosage on the effectiveness of bacterially induced carbonate precipitation on limestone. Ecological Engineering, 2010. **36**(2): p. 99-111.

22. Tracy, S.L., C.J.P. François, and H.M. Jennings, *The growth of calcite spherulites from solution: I. Experimental design techniques.* Journal of Crystal Growth, 1998. **193**(3): p. 374-381.

23. Al-Thawadi, S. and R. Cord-Ruwisch, Calcium carbonate crystals formation by ureolytic bacteria isolated from Australian soil and sludge. J. Adv. Sci. Eng. Res, 2012. **2**(1).

24. Andreassen, J.-P., et al., *Investigations of spherulitic growth in industrial crystallization.* Chemical Engineering Research and Design, 2010. **88**(9): p. 1163-1168.

25. Beck, R. and J.-P. Andreassen, *Spherulitic Growth of Calcium Carbonate.* Crystal Growth & Design, 2010. **10**(7): p. 2934-2947.

635 26. Mercedes-Martín, R., et al., Growing spherulitic calcite grains in saline,
636 hyperalkaline lakes: experimental evaluation of the effects of Mg-clays and organic
637 acids. Sedimentary Geology, 2016. **335**: p. 93-102.

638 27. Gunasekaran, S., G. Anbalagan, and S. Pandi, *Raman and infrared spectra of*
639 *carbonates of calcite structure.* Journal of Raman Spectroscopy, 2006. **37**(9): p. 892-899.

640 28. Anbu, P., et al., Formations of calcium carbonate minerals by bacteria and its
641 multiple applications. SpringerPlus, 2016. **5**: p. 250.

642 29. Agustawijaya, D., *The uniaxial compressive strength of soft rock.* Civil Engineering
643 Dimension, 2007. **9**(1): p. pp. 9-14.

644 30. Lian, C., Y. Zhuge, and S. Beecham, *The relationship between porosity and strength*
645 *for porous concrete.* Construction and Building Materials, 2011. **25**(11): p. 4294-4298.

646 31. Winter, N.B., Understanding Cement: An Introduction to Cement Production,
647 Cement Hydration and Deleterious Processes in Concrete. 2012: Microanalysis
648 Consultants.

649 32. Al-Thawadi, S.M., Consolidation of sand particles by aggregates of calcite
650 nanoparticles synthesized by ureolytic bacteria under non-sterile conditions. Journal of
651 Chemical Science and Technology, 2013. **2**(3): p. 141-146.

652